PAPER

Design and synthesis of novel pomegranate-like TiN@MXene microspheres as efficient sulfur hosts for advanced lithium sulfur batteries†

Mengjie Zhang,‡[a] Yang Lu, [ID] ‡*[a] Zhenjie Yue,[a] Mengmeng Tang,[a] Xiaoke Luo,[c] Chen Chen, [ID] [a] Tao Peng,[a] Xianming Liu [ID] [d] and Yongsong Luo [ID] *[ab]

Lithium–sulfur (Li–S) batteries have the characteristics of low cost, environmental protection, and high theoretical energy density, and have broad application prospects in the new generation of electronic products. However, there are some problems that seriously hinder the Li–S batteries from going from the laboratory to the factory, such as poor stability caused by the large volume expansion of sulfur during charging and discharging, sluggish kinetics of the electrochemical reaction resulting from the low conductivity of the active materials, and loss of active materials arising from the dissolution and diffusion of the intermediate product lithium polysulfides (LiPSs). In this paper, the two-dimensional layered material MXene and TiN are firstly combined by spray drying method to prepare pomegranate-like TiN@MXene microspheres with both adsorption capacity and catalytic effect on LiPSs conversion. The interconnected skeleton composed of MXene not only solves the problem of easy stacking of MXene sheets but also ensures the uniform distribution of sulfur. Without affecting the excellent characteristics of MXene itself, the overall conductivity of the composite electrode material is improved. The TiN hollow nanospheres are coated with MXene layers to form a shell, catalyzing the adsorption of LiPSs and accelerating the transformation of high-order LiPSs to Li_2S_2/Li_2S. As a result, the TiN@MXene cathode delivers a high initial discharge capacity of 1436 mA h g^{-1} at 0.1C, excellent rate performance of 636 mA h g^{-1} up to 3C, and an ultralong lifespan over 1000 cycles with a small capacity decay of 0.048% per cycle at the current density of 1.0C.

Introduction

The high quality requirements of electric vehicles and portable electronic devices have promoted the rapid development of energy storage technology.[1,2] Lithium–sulfur (Li–S) batteries have high energy density and high theoretical specific capacity (2600 W h kg^{-1} and 1675 mA h g^{-1}) due to the special 16-electron multistage conversion reaction of the sulfur cathode, which are much higher than those of lithium-ion batteries

widely used at present and are very attractive in various emerging high energy density power supplies.[3,4] However, Li–S batteries also have a series of obvious shortcomings, including the insulation of sulfur and terminal discharge products (Li_2S_2/Li_2S), the volume expansion during charge and discharge, and the shuttle effect of polysulfide.[5,6] To solve these problems, a lot of work has been done in the design of sulfur cathode materials. For example, carbon materials can significantly promote the electronic conductivity of sulfur cathodes, and the as-assembled Li–S cells displayed large specific capacities during the initial few cycles.[7,8] However, the weak physical interaction between polar LiPSs and non-polar carbon limits the adsorption of LiPSs by carbon-based cathode materials, which leads to the capacity attenuation in the later cycle.[9,10] Accordingly, sulfur host materials with both physical and chemical adsorption can effectively alleviate the shuttle effect of polysulfide and the decline of battery capacity. To improve the adsorption capacity of host materials for LiPSs and provide stronger chemical anchoring for LiPSs, various polar materials such as transition metal oxides,[11,12] metal sulfides,[13,14] and metal carbides[15] have been developed for sulfur host materials.

Among many materials, polar transition metal carbide nanosheets, like $Ti_3C_2T_x$ MXenes (T_x represents –O, –OH and –

[a] *Henan Joint International Research Laboratory of New Energy Storage Technology, Key Laboratory of Microelectronics and Energy of Henan Province, School of Physics and Electronic Engineering, Xinyang Normal University, Xinyang 464000, P. R. China. E-mail: luyang.181@163.com; ysluo@xynu.edu.cn; Fax: +86 376 6390801; Tel: +86 376 6390801*

[b] *College of Physics and Electronic Engineering, Nanyang Normal University, Nanyang 473061, P. R. China*

[c] *School of Information Engineering, Zhengzhou University, Zhengzhou 450001, P. R. China*

[d] *College of Chemistry and Chemical Engineering, Luoyang Normal University, Luoyang 471934, P. R. China*

† Electronic supplementary information (ESI) available. See DOI: https://doi.org/10.1039/d3ra00095h

‡ Mengjie Zhang and Yang Lu contributed equally to this work.

F) with abundant functional groups on its surface can provide sufficient binding energy for LiPSs generated during anchoring electrochemical reaction, thus avoiding the dissolution of LiPSs in electrolyte and the shuttle between cathode and anode.[3,5,16] As reported by Tang *et al.*, sulfate complexes formed by repeated cycling on the surface of MXene can be used as a protective barrier to effectively inhibit the shuttle effect and promote the utilization of sulfur.[17,18] In addition, MXene has excellent metal conductivity and rich active sites on the surface.[19] As a sulfur electrocatalyst, it ensures the rapid transmission of electrons and improves the redox reaction kinetics, thus accelerating the adsorption and catalytic conversion of LiPSs. Although MXene has so many advantages, as a two-dimensional layered material, it has a strong van der Waals force between layers, which leads to the easy stacking of peeled MXene nanosheets, which affects the specific surface area of MXene materials to reduce the exposed active sites and slows down the electron/ion transport during battery reaction.[20,21] The best way to solve this stacking problem is to assemble MXene with three-dimensional materials, or directly design MXene into three-dimensional structure.[22] Three-dimensional MXene not only does not lose the inherent properties of two-dimensional MXene but also increases the specific surface area of the material.[22,23] Moreover, it can have a good kinetic framework in both liquid and solid, ensuring the transmission of electrons/ions in the electrochemical reaction process.[24] In the electrochemical reaction process of lithium–sulfur batteries, the active edge was used to produce a certain amount of chemical adsorption on polysulfides to anchor the LiPSs generated in the electrochemical reaction process, reduce the dissolution of LiPSs in the electrolyte, and improve the utilization rate of active substance S.[23,25] For example, Wang *et al.* exposed more edge sites of 3D MXene by secondary etching method, and the experiment proved that the as-obtained MXene had a good adsorption catalytic effect on LiPSs.[16] However, a single polar trapper that simultaneously has strong adsorption ability and high catalytic activity toward LiPSs is hard to find. After a lot of literature research, we know that transition metal nitrides not only have good electrical conductivity but also have excellent electrocatalytic effects to reduce the reaction barrier of LiPSs conversion and accelerate the electrochemical reaction.[26] Huang *et al.* have studied carbon wrapped titanium nitride nanomesh (TiN NM@C) and used it as S cathode of Li–S battery, which showed excellent electrochemical performances owing to the adsorption and catalysis of TiN.[27] Peng *et al.* prepare MXene-derived TiN nanoflakes as sulfur host and study the catalytic action, which demonstrate that the (001) facet-dominated TiN nanoflakes have a strong adsorption capacity for LiPSs.[28] Nevertheless, only a few studies about TiN with hollow structure applied as sulfur hosts have been reported due to the limited preparation strategies and technologies. Therefore, the design of MXene/TiN composite materials with more edge sites can accelerate electron/ion transport, improve the catalytic effect of the material on LiPSs, and further improve the utilization rate of the active substance sulfur.

Here, a facile strategy to prepare 3D pomegranate-like TiN@MXene microspheres is reported for the first time. The microspheres were prepared by a simple spray drying method with MXene as "pomegranate peel" and TiN as "pomegranate seed". Spray drying technology assembles MXene nanosheets into three-dimensional microspheres, which solves the problem of self-stacking, while retaining their own advantages. The MXene skeleton and coating layer ensures the overall conductivity of the material. Hollow TiN nanospheres wrapped by "pomegranate peel" MXene have a good catalytic effect on the transformation of high-order LiPSs to Li_2S_2/Li_2S, which can lower the reaction energy barrier to accelerate the conversion process. Moreover, TiN@MXene composite has a large specific surface area, which can alleviate the problem of sulfur volume expansion during charge and discharge. Based on the above advantages, the TiN@MXene/S cathode ensures the electrochemical performance of lithium–sulfur batteries, which can provide a discharge capacity of up to 1436 mA h g^{-1} at 0.1C. At the same time, the discharge capacity remains 474 mA h g^{-1} after 1000 cycles at a 1C charge–discharge rate, and the capacity fading rate is only 0.048%. This study provides an ingenious design strategy for the synergistic integration of MXene (Ti_3C_2) materials with excellent performance and TiN with accelerated LiPSs catalytic conversion, which will contribute to the innovative design of lithium–sulfur batteries with excellent performance in the future.

Experimental section

Synthesis of sulfonated polystyrene (sPS) spheres

A single-dispersed polystyrene geometric cell was synthesized by free-form emulsion polymerization. In a classic synthesis process, first of all, with 0.1 M sodium hydroxide solution to wash off the styrene blocker, with a dropper to the upper layer of golden liquid added to the deionized water washed to neutral, take 32 mL washed golden liquid and 320 mL of deionized water added to the three-necked flask. Then, the reaction flask was heated to 80 °C in an Ar atmosphere. After stirring for 30 minutes, 0.2 g of potassium persulfate was dissolved in 10 mL of deionized water, and then the resulting solution was added to the three-necked flask. After mixing for 10 h, the product was washed with deionized water and freeze-dried. The dried polystyrene powder (3 g) was mixed with concentrated sulfuric acid (98%, 30 mL), and the mixture was stirred at room temperature for 24 h. Finally, the sulfonated polystyrene (sPS) nanospheres were washed with ethanol and freeze dried.

Synthesis of sPS@TiO$_2$

First, 1 g of sPS spheres was dispersed in 40 mL of absolute ethanol, and the homogeneous solution was formed by ultrasonic stirring for 1 h. 1.2 mL of tetrabutyl titanate was slowly added to the solution by using a propeller, and 1.2 mL of deionized water was slowly added after stirring for 0.5 h. After stirring at room temperature for 10 h, the solution was washed several times with deionized water and absolute ethanol to obtain the white product which was freeze-dried into powders. The prepared sPS@TiO$_2$ spheres were dispersed in 50 mL of deionized water.

Synthesis of Ti₃C₂Tₓ nanosheets

The $Ti_3C_2T_x$ powder was obtained by stripping off the aluminum layer from commercially available Ti_3AlC_2 powder using an acid etching solution. 1 g of LiF was added to 20 mL of 9 M of hydrochloric acid under vigorous stirring, and then 5 mL of 40% HF was added and the mixture was magnetically stirred until the solution became clear. 1 g Ti_3AlC_2 powder was added slowly for 1 h. After 12 h of magnetic stirring, the reaction mixture was washed repeatedly with deionized water until it was close to neutral. After centrifugation at 8500 rpm for 1 h, the supernatant was collected, and the concentration was about 2.0 mg mL^{-1} MXene solution.

Synthesis of pomegranate-like TiN@MXene and TiN@MXene/S composites

50 mL sPS@TiO₂ was added to 100 mL of MXene solution (2 mg mL^{-1}) and sonicated for 1 h. The mixture was spray-dried at 140 °C in air with a feed rate of 600 mL h^{-1}. Afterwards, the obtained sPS@TiO₂@MXene and melamine were placed separately in two crucibles. The crucible with sPS@TiO₂@MXene was placed under the heating wire of the furnace, and the crucible with melamine was placed on the top of the furnace and beside the crucible containing sPS@TiO₂@MXene (w/w, 1 : 1). The powders were heated in argon atmosphere according to the heating rate of 2 °C min^{-1}, kept at a constant temperature of 300 °C for 2 h, then raised to 800 °C for 2 h, and finally cooled to room temperature naturally to obtain TiN@MXene composite. The TiN@MXene/S composites were prepared by mixing sulfur and TiN@MXene powders, which were transferred to a polytetrafluoroethylene container, filled with argon gas, and treated at 155 °C for 12 h. The 3D-MXene/S was obtained by spray-dried and sulphureting in the same way as preparing TiN@MXene/S. To simplify the description, in the text of the part about electrochemical performance, we refer to TiN@MXene/S and 3D-MXene/S electrodes as TiN@MXene and 3D-MXene cathode, respectively.

Characterization

The morphologies and the corresponding elemental maps of the samples were characterized on the Hitachi S-4800 scanning electron microscope (SEM) and FEI Tecnai G2 F20 transmission electron microscope (TEM). X-ray diffraction (XRD, Bruker D8 Advance system, Cu-Kα, $\lambda = 1.5418$ Å) was used to identify the crystal phase of the samples. The chemical elements and bonding characterizations were analyzed on an X-ray photoelectron spectroscopy (XPS, PerkinElmer model PHI 5600). The thermogravimetric analysis (TGA) curves were surveyed on a STA499F5 analyzer. The nitrogen adsorption/desorption isotherms and surface areas were conducted by Brunauer–Emmett–Teller analysis on a physical & chemical adsorption system (ASAP 2460) at the constant temperature of 77 K. The ultraviolet-visible (UV-vis) absorption test was recorded on the U-3900H spectrophotometer (Hitachi, Japan). The optical images were taken using a Sony camera.

Electrochemical measurements

The TiN@MXene/S composites, carbon black and polyvinylidene fluoride (PVDF) were added into N-methyl-2-pyrrolidone (NMP) in a weight ratio of 8 : 1 : 1 to prepare cathode slurry. The slurry was spread on an aluminum foil, dried in a vacuum at 60 °C. The CR2032 coin cells with the lithium metal sheet, Celgard 2400 separator and the above composite cathodes were assembled in glovebox. The electrolyte was composed of 1 M lithium bis-trifluoromethanesulfonylimide (LiTFSI) dissolved in a mixture of 1,3-dioxolane (DOL)/1,2-dimethoxyethane (DME) (volume ratio = 1 : 1) with 1 wt% LiNO₃. The areal sulfur loadings of the cathodes were controlled to be between 1.0 and 1.4 mg cm^{-2} for testing, and a high sulfur loading of 5.1 mg cm^{-2} was also employed to evaluate the potential in practical applications. The specific capacity was calculated based on the weight of sulfur. For low sulfur loading cathodes, 30 μL electrolyte was added and the electrolyte/sulfur ratio is 13.63 μL mg^{-1}. And for high loading cathodes, the usage of electrolyte is 60 μL, where the electrolyte/sulfur ratio is 14.98 μL mg^{-1}. Before performing the electrochemical performance test, the cells were placed at room temperature for 8 hours to ensure complete penetration of the electrolyte. VMP3 multi-channel electrochemical workstation (Bio-Logic) was used to measure cyclic voltammetry (CV) curves at different scanning rates in the range of 1.7–2.8 V. The electrochemical impedance spectroscopy (EIS) was measured by using CHI660E electrochemical workstation, the test frequency was between 100 kHz and 10 MHz, and the test temperature was 25 °C. The galvanostatic charge–discharge (GCD) tests were carried out between 1.7 and 2.8 V on a Netware battery-testing system based on different densities.

Polysulfide adsorption performance

The polysulfide (Li₂S₆) solution was synthesized by dissolving S powder and Li₂S at a molar ratio of 5 : 1 in DOL and DME (1 : 1, ratio by volume). 20 mg of the sample (3D-MXene or TiN@MXene) was added to 5 mL Li₂S₆ solution (5 mmol L^{-1}), stirred vigorously to facilitate adsorption and monitored color change at any time. The color change of the solutions was recorded by an optical camera and a glass vial filled with the bare Li₂S₆ solution was used as a comparison. All the procedures were performed in an Ar-filled glovebox.

Symmetric cell test

The 3D-MXene and TiN@MXene were loaded on carbon paper as the electrode (the mass loading was 0.5 mg cm^{-2}). Li₂S₆ and sulfur powder with a molar ratio of 5 : 1 was dissolved in DOL/DME solution containing 1 mol L^{-1} LiTFSI and 0.1 mol L^{-1} LiNO₃ (volume ratio 1 : 1) to prepare 0.2 mol L^{-1} Li₂S₆ solution. Two identical electrode plates were assembled into a button cell using a Celgard 2500 separator and a 20 μL Li₂S₆-based electrolyte. The CV measurements were tested by the CHI660E workstation.

Li$_2$S nucleation test

Li$_2$S$_8$ solution was prepared by dissolving Li$_2$S and S with a molar ratio of 1 : 7 into Li–S electrolyte under vigorous stirring at 60 °C for 24 h. The 3D-MXene or TiN@MXene sample was loaded on carbon paper as a cathode (the mass loading was 1 mg cm^{-2}), and Li foil was used as an anode for the test. Carbon paper loaded with TiN@MXene or 3D-MXene dispersed in Li$_2$S$_8$ electrolyte was used as cathode, and the Li foil was applied as anode and about 25 μL of blank Li–S electrolyte was dropped on the anode. The batteries were first discharged to 2.09 V under a constant current of 0.112 mA, and then discharged potentiostatically at 2.08 V until the current was below 0.01 mA.

Results and discussion

In this work, the synthesis process of hollow pomegranate-like TiN@MXene microspheres is shown in Fig. 1. Sulfonated polystyrene (sPS) nanospheres with an average size of 300 nm were selected as templates (Fig. S1†). Initially, few-layered Ti$_3$C$_2$T$_x$ nanosheets (Fig. S2b†) were prepared by the targeted etching and exfoliation of Ti$_3$AlC$_2$ MAX phase (Fig. S2a†),[29] TiO$_2$ was coated on the surface of sPS by a deposition method. Then, the sPS@TiO$_2$ nanospheres (Fig. S3a†) were dispersed into MXene aqueous solution, followed by ultrasonication and vigorous stirring. The mixture solution was pumped into a spray dryer quickly, and further the sPS@TiO$_2$@MXene composites were obtained. Subsequently, the product was calcined at 300 °C for 2 h to remove sPS and built a porous structure, thus increasing the specific surface area of the composite.[30] Finally, TiN@MXene composites were prepared by nitridation of TiO$_2$@MXene with melamine in the Ar atmosphere. To obtain an ideal sulfur host material, sulfur was encapsulated into the TiN@MXene spheres *via* a melt-diffusion process to obtain the TiN@MXene/S composite.

Scanning electron microscope (SEM) images and transmission electron microscope (TEM) images of the as-obtained samples at various stages are shown in Fig. 2. The obtained sPS@TiO$_2$ was mixed with MXene and spray dried, which contributes to a regular, pomegranate-like microsphere

assembly with sPS@TiO$_2$ nanospheres firmly and fully wrapped by the wrinkled MXene nanosheets (Fig. 2a). It can be seen from the graph that MXene uniformly covers sPS nanospheres with a diameter of about 300 nm, forming pomegranate-like microspheres with a diameter of 4–5 μm. Hollow porous MXene microspheres (3D-MXene) can be obtained by annealing sPS@MXene microspheres in the Ar atmosphere (Fig. 2b). Fig. 2d shows the TEM image of 3D-MXene with typical porous structure, manifesting the successful removal of sPS from sPS@MXene composites. This interconnected network structure not only effectively avoid the self-stacking of MXene, but also facilitate the uniform loading of sulfur on the host material. Since MXene has good conductivity, this three-dimensional skeleton can also promote the transmission of electronic ions in the battery reaction.[5,31]

The exposed edge sites have a certain adsorption effect on the LiPSs generated in the battery reaction, which reduces the amount of LiPSs dissolved in the electrolyte and improves the utilization rate of sulfur. On the one hand, the porous structure is conducive to the penetration of electrolytes, and on the other hand, it is also conducive to alleviating the sulfur volume expansion during the charge and discharge processes. Tetrabutyl titanate was selected as the titanium source, and sPS@TiO$_2$ (Fig. S3a†) was synthesized by coating a layer of TiO$_2$ on the surface of sPS *via* a hydrolysis coating method. The 3D sPS@TiO$_2$@MXene architecture (Fig. S3b†) was fabricated by spray drying of MXene solution using sPS@TiO$_2$ as a template. Then, TiN@MXene microsphere (Fig. 2c) was gained by removing sPS and annealing TiO$_2$ into TiN using melamine as N source in Ar atmosphere. Combined with the TEM image of TiN@MXene (Fig. 2e), it is found that TiN retains accordant spherical void spaces with a diameter of about 300 nm, resulting from the thermo-decomposition of sPS. The TiN shell ~20 nm in thickness wrapped in MXene sheets (Fig. 2f and g), proving that TiN hollow spheres and MXene sheets successfully assembled pomegranate-like structure. The high-resolution transmission electron microscopy (HRTEM) of the TiN@MXene sample shows the lattice fringes with spacing of 0.243 nm attributing to the (111) plane of TiN (Fig. 2h).[27,30] TiN@MXene/S and 3D-MXene/S composites were prepared by the melt sulfur
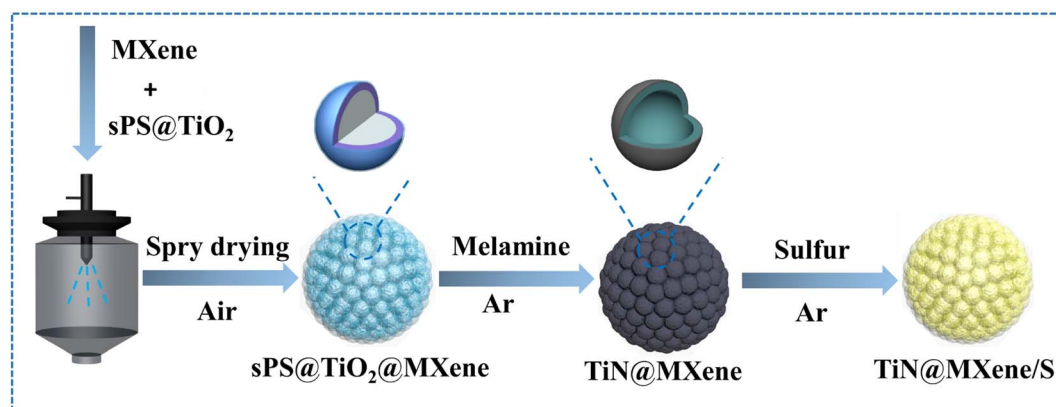

Fig. 1 Schematic illustration of the synthesis process of TiN@MXene/S.

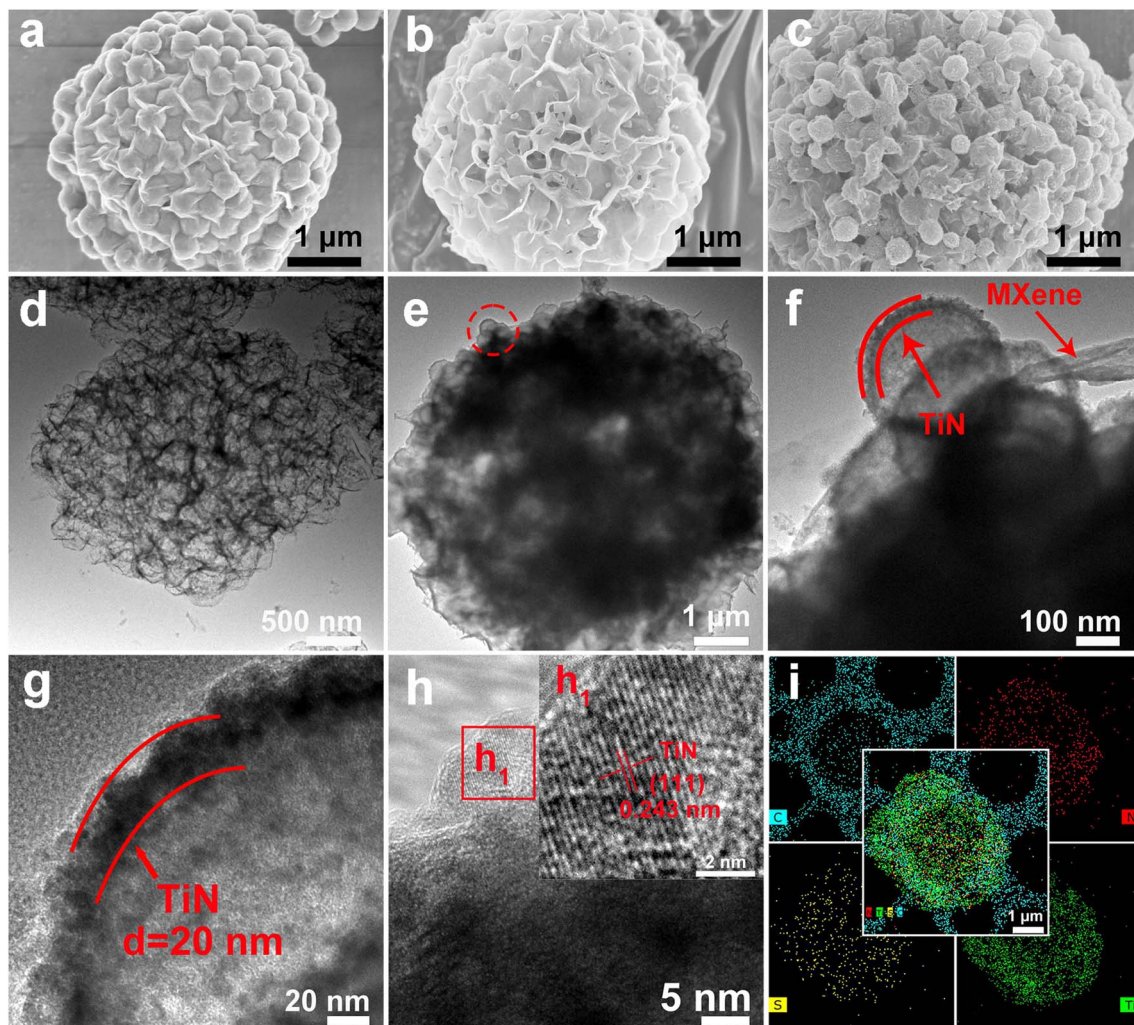**Fig. 2** SEM images of (a) sPS@MXene, (b) 3D-MXene, (c) TiN@MXene. (d) TEM image of 3D-MXene. (e)–(g) TEM images and (h), (h₁) high-resolution TEM image of TiN@MXene. (i) Mapping image of TiN@MXene/S and the corresponding elemental mappings of C, Ti, N, and S.

fixation method according to the ratio of 7 : 3. The sulfur content of the two composites is 68.55% and 68.73% respectively, using the thermogravimetric analysis (Fig. S4c and d†). Their corresponding XRD patterns after sulfur was incorporated are shown in Fig. S4b,† which display typical peaks indexed to S_8 (JCPDS: 08-0247). In addition, energy-dispersive X-ray spectroscopy (EDS) element mapping demonstrates the homogeneous distribution of Ti, S, N, and C throughout the TiN@MXene/S microspheres (Fig. 2i), which further validates that TiN, sulfur and MXene are uniformly distributed in the microspheres. Unlike 3D-MXene, TiN@MXene not only has a MXene skeleton to improve the conductivity of the material and exposes the MXene lamellar edge to adsorb LiPSs generated during the battery reaction, but also has a hollow TiN nanosphere with good catalytic performance to achieve the adsorption catalysis of LiPSs.

The phase characteristics of the as-prepared samples are surveyed by XRD. The XRD results of Ti_3AlC_2 MAX phase powders and multilayered $Ti_3C_2T_x$ MXenes are shown in Fig. S4a.† The (002) peak widens and migrates to lower angle compared with the MAX phase, directly suggesting that the well-exfoliated MXene is successfully prepared.[32,33] After a spray-drying process, a sharp (002) peak for 3D-MXene at 6.8° besides weak (006) and (008) peaks of $Ti_3C_2T_x$ could be observed (Fig. 3a), but no peaks of anatase or rutile type TiO_2 appear, demonstrating good stability of MXene in the synthesis process. Apart from the peaks of $Ti_3C_2T_x$, five peaks of TiN at (111), (200), (220), (311) and (222) also appear in TiN@MXene, indicating the successful introduction of TiN in TiN@MXene composites (JCPDS No. 87-0632).[34,35] This corresponds well to the lattice spacing of TiN measured in the HRTEM of the TiN@MXene sample. The 3D-MXene and TiN@MXene have obvious holes and caves, which were further verified by nitrogen adsorption–desorption experiments. The N_2 adsorption–desorption curves of samples are in line with the type-IV isotherm (Fig. 3b), indicating that both the samples are mesoporous materials, which is consistent with the pore size distribution (Fig. 3c). The specific surface areas of 3D-MXene and TiN@MXene are 97.69 $m^2\ g^{-1}$ and 181.38 $m^2\ g^{-1}$, respectively, according to the simulation calculation combined with the isothermal line. The
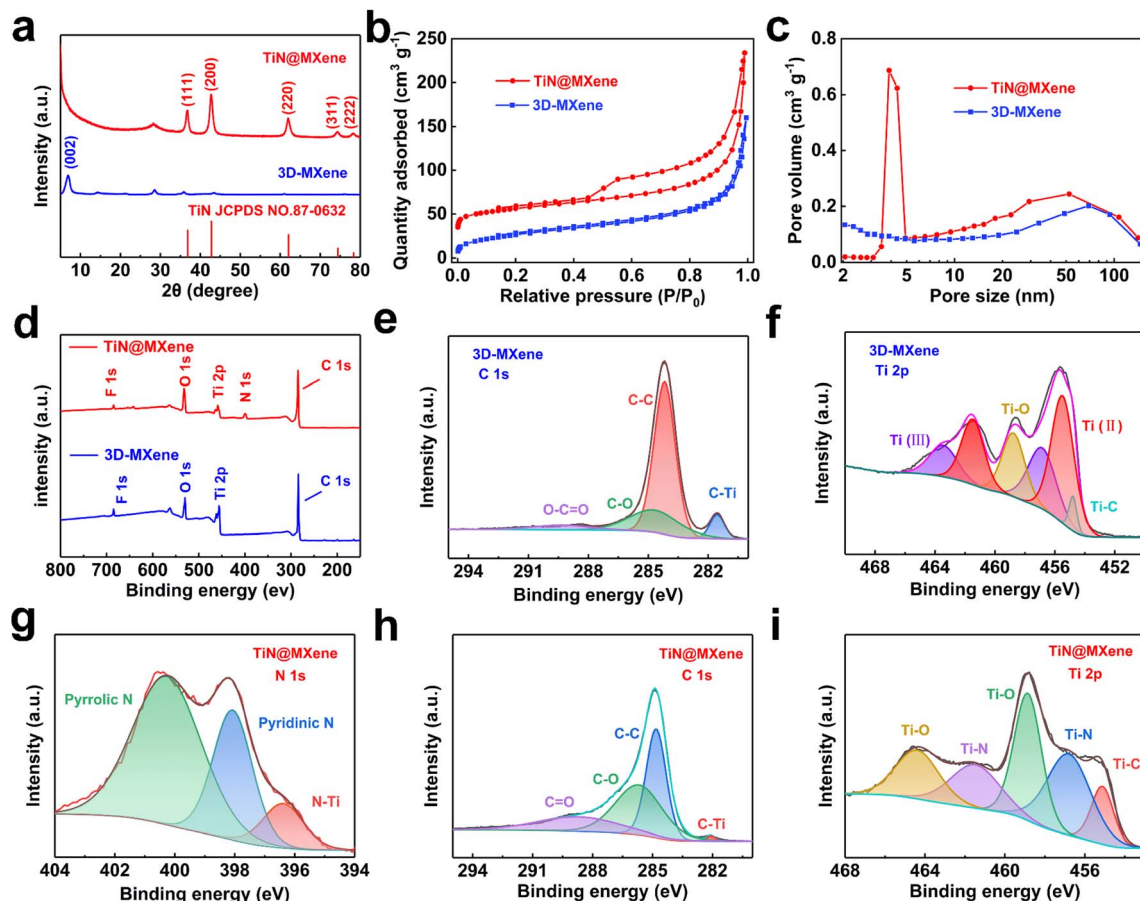
Fig. 3 (a) XRD patterns of 3D-MXene and TiN@MXene. (b) Nitrogen adsorption–desorption isotherms and (c) BJH pore-size distribution diagrams of 3D-MXene and TiN@MXene. (d) XPS survey spectra of 3D-MXene and TiN@MXene. (e) and (f) High-resolution XPS spectra of C 1s and Ti 2p for 3D-MXene, respectively. (g)–(i) High-resolution XPS spectra of N 1s, C 1s and Ti 2p for TiN@MXene, respectively.

incremental surface area of TiN@MXene is the result of the additional TiN hollow spheres, which is beneficial to affording aggregation-resistant property within TiN@MXene and allowing the enough sulfur infiltration and electrolytic accessibility, thus contributing to overall electrochemical performance.

Fig. 3d–i is the X-ray photoelectron spectroscopy of 3D-MXene and TiN@MXene. The total element distribution of the two materials can be seen from the total spectrum. The F element in the two materials comes from the LiF used in the etching of MXene. Different to 3D-MXene, TiN@MXene contains N element. Fig. 3e and h show the energy spectra of C 1s of 3D-MXene and TiN@MXene, respectively. C 1s in 3D-MXene can be fitted to four peaks: C–Ti (281.5 eV), C–C (284.4 eV), C–O (284.6 eV), and O–C=O (288.5 eV).[36] The signals of the C–Ti peak are mainly from C and Ti in MXene, and C–C is mainly from graphite C in the formation process of MXene. Compared with 3D-MXene, the peak fitted by C 1s of TiN@MXene shifts to high binding energy as a whole, and the strength of the C–Ti bond from MXene decreases, which may be related to the formation of TiN.[1] The Ti 2p of 3D-MXene (Fig. 3g) could fit the following peaks: 454.8 eV, 455.42 eV, 456.85 eV, 458.9 eV, 461.48 eV, and 463.45 eV. Among them, 454.8 eV corresponds to the Ti–C bond, 455.42 eV and 461.48 eV correspond to Ti (II)

bond, 456.85 eV and 463.45 eV correspond to Ti (III) bond, 458.9 eV reflects to Ti–O bond, which may be due to the bonding of oxygen-containing functional groups on the surface of MXene.[37] After TiN adding, the bonding of TiN@MXene Ti 2p changed (Fig. 3i). In addition to Ti–O and Ti–C bonds, Ti combined with N to form a new Ti–N bond.[38] Fig. 3g shows the spectrum of N 1s in TiN@MXene can be identified to three peaks at 400.09 eV, 398.10 eV, and 396.48 eV, corresponding to pyrrolic N, pyridinic N, and Ti–N bonds, respectively.[1] It is reported that pyridine nitrogen and pyrrole nitrogen can effectively improve the strong Lewis acid–base interaction between polar titanium atoms and elemental sulfur (S_8) and LiPSs (Li_2S_n affinity and binding energy $4 \leq n \leq 8$).[39]

The adsorption of LiPSs on the catalyst surface is a necessary condition for inhibiting the shuttle effect and boosting the catalytic redox process.[40] To reveal the chemisorptive nature of 3D-MXene and TiN@MXene for LiPSs, the visualized decoloration tests were adopted by soaking samples in Li_2S_6 solution (Fig. 4a). The Li_2S_6 solution containing TiN@MXene became completely colorless after 12 h of reaction, while the solution with 3D-MXene displayed slight color fading, indicating that some Li_2S_6 was still left in the solution. Simultaneously, the UV-vis spectra (Fig. 4b) demonstrate the most dramatic decline of
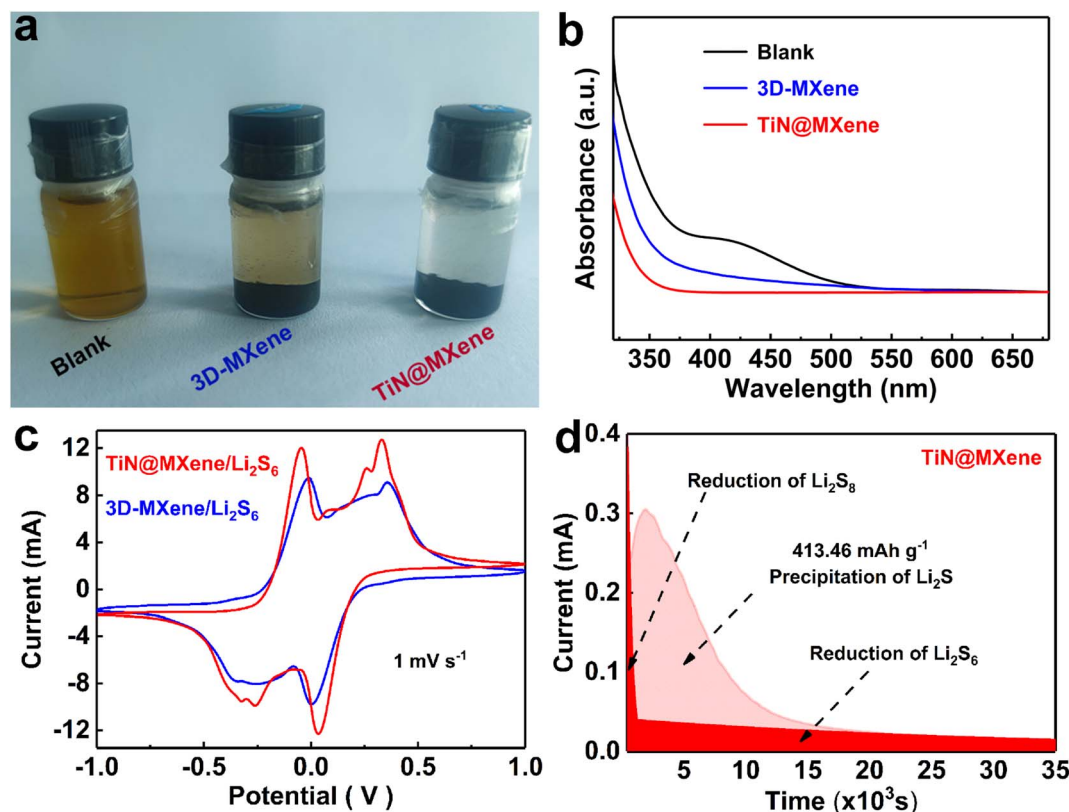
Fig. 4 (a) Photograph of Li_2S_6 adsorption test with 3D-MXene and TiN@MXene composites. (b) Ultraviolet-visible absorption spectra of Li_2S_6 solution and ones after adding 3D-MXene and TiN@MXene. (c) CV curves of symmetrical batteries using 3D-MXene and TiN@MXene electrodes. (d) Constant potential discharge curve of the Li_2S deposition tests using TiN@MXene as substrate.

the absorbance intensity for the TiN@MXene, indicating the adsorption of the Li_2S_6 species by TiN@MXene is much stronger than 3D-MXene.

To verify the positive effect of 3D-MXene and TiN@MXene materials on the redox kinetics of LiPSs, symmetrical batteries were assembled using different samples loaded on carbon paper (CP) as electrodes and 0.2 M Li_2S_6 as electrolyte.[41] The voltage range was −1.0–1.0 V at a 1 mV s^{-1} scanning rate. The tested samples showed clear cyclic voltammetry peaks at both cathode and anode, which identified the LiPSs conversion. Dramatically, the TiN@MXene sample displays a higher redox current and larger closed CV area than that of 3D-MXene, suggesting the significantly promoted liquid-phase catalytic activity.[40] CV evaluation of symmetric batteries verified that the catalytic effect of TiN@MXene significantly improved the reaction kinetics of liquid polysulfides. Meanwhile, Li_2S precipitation experiments were carried out to probe the liquid–solid transformation characteristics of the electrode surface.[42] Li_2S_8 electrolyte replacing S_8 active material was added to simulate the real state of the lithium–sulfur system. The time-response current truly recorded the entire Li_2S electrodeposition process.[43] As shown in Fig. 4d, the *I*–*t* plot can be divided into three blocks: the initial reduction of Li_2S_8, the precipitation of Li_2S and the reduction of Li_2S_6. Compared with the 3D-MXene electrode (Fig. S5†), TiN@MXene displays a higher current response and the peak states the precipitation of Li_2S.

According to Faraday's law, the capacity of precipitated Li_2S on TiN@MXene (413.46 mA h g^{-1}) is much larger than that of 3D-MXene (222.78 mA h g^{-1}), which proves that TiN promotes the conversion of LiPSs to Li_2S. The above experimental results prove that TiN@MXene can effectively catalyze the electrochemical conversion of LiPSs, stimulate the hysteresis multiphase redox kinetics during charge and discharge, and finally improve the overall electrochemical performance of the Li–S battery.[44]

To systematically evaluate the electrochemical properties, the comparison of CV curves of TiN@MXene and 3D-MXene cathodes at 0.1 mV s^{-1} was shown in Fig. 5a. In the cathodic scan process, a pair of cathodic peaks correspond to the reduction of sulfur to long chain LiPSs (I), and the further reduction of LiPSs towards short-chain Li_2S_2/Li_2S (II), respectively. In the succeeding anodic scan, the characteristic peaks were derived from the reversible oxidation of Li_2S_2/Li_2S to LiPSs, and subsequently to sulfur (III).[45] It can be clearly observed that compared with 3D-MXene, TiN@MXene cathode shows greater current response and lower polarization, indicating the fast Li$^+$ transport and a boosted redox kinetic process. The Li$^+$ diffusion coefficient can directly reflect the kinetics of LiPSs. Therefore, the CV plots (Fig. 5b and c) were further recorded at different scan rates to inspect the Li-ion diffusion coefficient of the sulfur cathodes according to the Randalls–Sevcik (R–S) equation:[46]
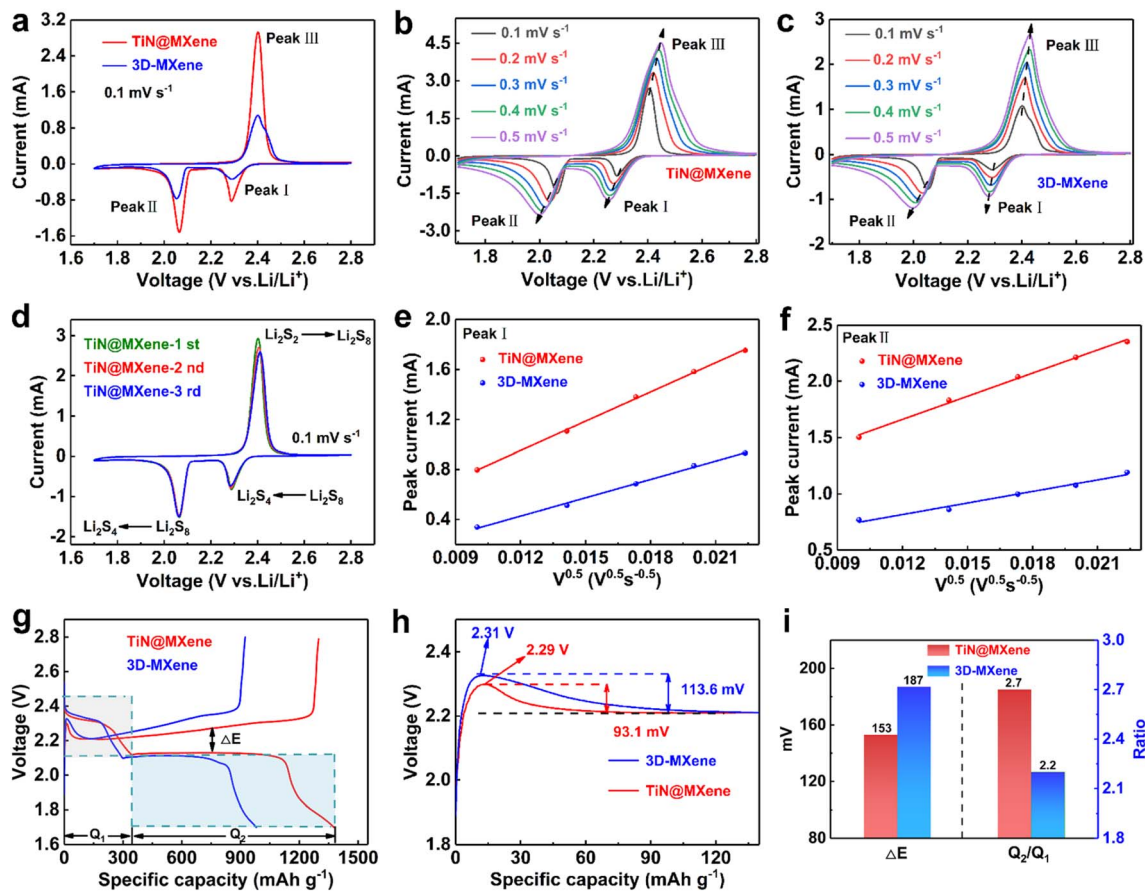
Fig. 5 (a) CV curves of TiN@MXene and 3D-MXene cathodes in the range of 1.7–2.8 V at 0.1 mV s^{-1}. (b) and (c) CV curves of TiN@MXene and 3D-MXene cathodes at various scan rates. (d) Scan of TiN@MXene cathode at 0.1 mV s^{-1} for different numbers of revolutions. (e) and (f) The corresponding linear fits of the peak currents for Li–S batteries. (g) The initial charge–discharge profiles at 0.1C. (h) The amplification platform of charging curve. (i) ΔE and Q_2/Q_1 values obtained from charging/discharging curves.

$$I_{peak} = (2.69 \times 10^5)n^{1.5}AD_{Li}^{0.5}v^{0.5}C_{Li} \tag{1}$$

Specifically, I_{peak} is the slope of the linear plot of the peak current, n is the number of electrons in the reaction ($n = 2$ in Li–S batteries), A is the area of the electrode (2 cm^2), D_{Li} is diffusion coefficient of Li-ions, v is the scan rate and C_{Li} is the molar concentration of Li-ions in the electrode (0.55 mol L^{-1}). The linear plots of the peak current (I_{peak}) *versus* the square root of the scan rate ($v^{0.5}$) were received by reading data on the CV curves of diverse scanning rates (Fig. 5e and f). The two cathodic peaks are marked as I and II, while the anodic peak at higher voltage is marked as III. Based on the R–S equation and the curves of I_{peak}–$v^{0.5}$, the diffusion coefficient can be obtained after calculation and the results are presented in Table S1.† At the stage from S to long-chain LiPSs corresponding to peak I, the D_{Li} on TiN@MXene (8.72×10^{-9} cm^2 s^{-1}) is larger than that on 3D-MXene (3.40×10^{-9} cm^2 s^{-1}). At peak II, which represents the next discharge stage from the soluble lithium polysulfides to Li$_2$S/Li$_2$S$_2$, the D_{Li} on TiN@MXene (6.73×10^{-9} cm^2 s^{-1}) is still much larger than that on 3D-MXene (1.68×10^{-9} cm^2 s^{-1}). Additionally, the oxidation peak of III also presents a similar trend (Fig. S6†). At the same time, the TiN@MXene

cathode also displays lower ohmic resistance and charge transfer resistance indicating fast synergetic catalytic conversion of LiPSs by the TiN@MXene host (Fig. S7†). As stated above, TiN@MXene cathode represented superior diffusion and possessed better reaction kinetics compared with the single 3D-MXene cathode, verifying that TiN@MXene could boost the polysulfide redox kinetics in terms of sulfur reduction and oxidation reactions benefited from the presence of catalytic sites TiN. Fig. 5d compares the CV curves of different cycles of the TiN@MXene cathode at 0.1 mV s^{-1}. In succeeding cycles, the redox peaks almost overlap those in the 1st cycle and no marked difference in the intensities and corresponding potentials of the peaks is observed, proving the excellent electrochemical stability.

The capacity difference in the charge–discharge process is mainly due to the rearrangement of sulfur and the incomplete conversion between long-chain LiPSs and the final discharge product Li$_2$S, while the sulfur hosts with excellent performance can promote the reaction kinetics of liquid–solid conversion.[47] Fig. 5g plots the constant current charge–discharge curves of the batteries prepared by the 3D-MXene and TiN@MXene cathode at 0.1C. Both cathodes exhibit one charging platform
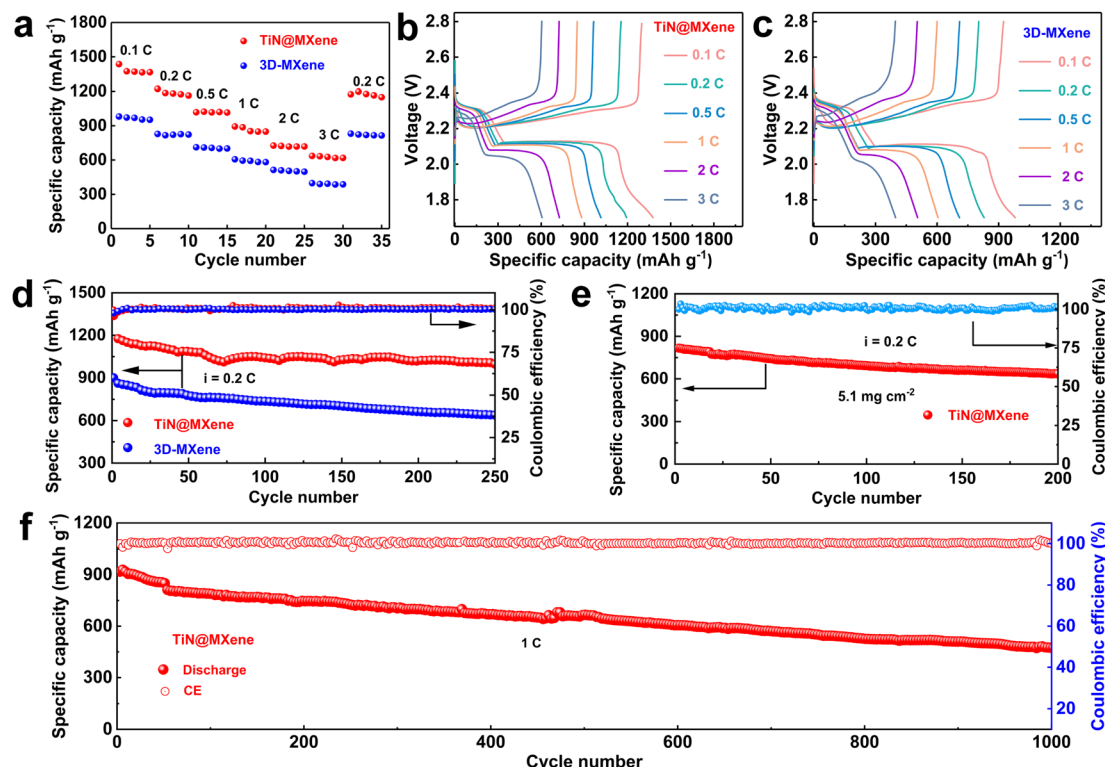
Fig. 6 (a) Rate performance for the 3D-MXene and TiN@MXene cathodes at various current densities. (b) and (c) Galvanostatic charge–discharge profiles of the TiN@MXene cathode and 3D-MXene cathode at various current densities. (d) Cycling stabilities of the TiN@MXene and 3D-MXene cathodes at 0.2C. (e) Cycling performance of the battery with TiN@MXene cathode at high sulfur loading. (f) Long-term cycling stability at 1C of the TiN@MXene cathode.

and two discharging platforms, consistent with the measured CV peaks (Fig. 5a). Compared to the initial capacity of the cathode with 3D-MXene (980 mA h g^{-1}), the TiN@MXene cathode displays much larger capacity of 1376 mA h g^{-1}. Moreover, we measured the polarization potential (ΔE) between the charging and discharging plateau in Fig. 5i, the TiN@MXene cathode reveals a smaller plateau voltage gap ($\Delta E = 153$ mV) than the 3D-MXene ($\Delta E = 187$ mV) cathode. During the discharge course, the discharge capacity in the stage of the transformation of sulfur to soluble LiPSs (Q_1) and the following conversion to insoluble Li_2S_2/Li_2S (Q_2) was 368 and 1008 mA h g^{-1} for the TiN@MXene cathode, respectively, which was higher than that of the 3D-MXene cathode ($Q_1 = 306$ mA h g^{-1}, $Q_2 = 674$ mA h g^{-1}). The Q_2/Q_1 ratio of the TiN@MXene cathode was also larger than that of the 3D-MXene cathode (Fig. 5i). Above all the test results strongly prove that TiN@MXene cathode has a faster LiPSs conversion kinetics and a higher reversibility of sulfur redox reactions. We analyzed the decomposition energy barrier of Li_2S by surveying the charging curves (Fig. 5h). The Li_2S decomposition barrier of TiN@MXene cathode was 2.29 V, which was lower than that of 3D-MXene cathode (2.31 V), suggesting the greater catalytic activity of TiN@MXene. Additionally, the potential difference between the Li_2S decomposition point and the charge platform of TiN@MXene, 3D-MXene was 93.1 and 113.6 mV, respectively, further

attesting the faster reaction kinetics for TiN@MXene cathode (Fig. 5h).

Since TiN@MXene has high adsorption and catalytic capacity for LiPSs, the Li–S batteries prepared with TiN@MXene cathode shows good electrochemical performance, especially compared with the 3D-MXene cathode. The rate performance of TiN@MXene and 3D-MXene cathodes was observed when the current density increased from 0.1 to 3C (Fig. 6a–c). The TiN@MXene cathode attained discharge capacities of 1436, 1221, 1018, 893, 726 and 636 mA h g^{-1} at 0.1, 0.2, 0.5, 1, 2 and 3C, respectively. The discharge capacity of 1174 mA h g^{-1} was achieved when the current density returned to 0.2C, proving the excellent stability of the cathode at various rates. By comparison, the battery assembled with 3D-MXene cathode displayed smaller capacities of 980, 828, 711, 606, 513 and 397 mA h g^{-1} at the same rate. Fig. 6b plots the GCD curves of the TiN@MXene cathode under increasing rates from 0.1 to 3C. The discharge curves included two discharge plateaus at around 2.3 and 2.1 V, which correspond to the conversion of S_8 to LiPSs and further to form Li_2S, respectively.[48] Even at the high discharge rate of 3C, we can still clearly observe two obvious reductive plateaus, which means that the TiN@MXene cathode was able to achieve outstanding redox reaction kinetics. The rate performance was much superior to those of the previously reported cathodes based on TiN or some other catalytic materials for Li–S batteries (Fig. S8†).[49–52]
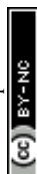
The cycling performances of the two cathodes at 0.2C over 250 cycles are plotted on Fig. 6d. The TiN@MXene cathode achieved an initial discharge capacity of 1185 mA h g^{-1} with a coulombic efficiency of 99.5% and maintained a capacity of 996 mA h g^{-1}, with a capacity decay of 0.064% per cycle. In contrast, the 3D-MXene cathode presents a much lower specific capacity with a remanent capacity of 638 mA h g^{-1} after 250 cycles, which corresponds to approximately 70% of the initial value. In Fig. 6e, the TiN@MXene cathode with a high S content of 5.1 mg cm^{-2} displays a relatively large specific capacity (816 mA h g^{-1}) at 0.2C after 200 cycles approaching 77% of the initial capacity, indicating the good application prospect in the field of Li–S batteries. To further investigate the cyclic stability, Fig. 6f displays the long cycling performance of TiN@MXene cathode at 1C. The discharge capacity is retained at 474 mA h g^{-1} after 1000 cycles. It is noteworthy that the corresponding capacitance retention was 52%, amount to a small decay rate of 0.048% per cycle, and a coulombic efficiency of nearly 100% in the whole cycles. In short, TiN@MXene cathode with the synergetic effect on anchoring and converting soluble LiPSs can perform outstanding cycling performance even at high S loadings. To investigate whether TiN@MXene itself contributes to the capacity of the battery, we assembled and tested a half-cell with metal lithium and TiN@MXene with no active material (S). The cycle performance of the TiN@MXene half-cell at 0.2 mA proves that TiN@MXene does not provide capacity during cycles in the Li–S batteries (Fig. S9†).[53]

Conclusions

To obtain the multi-functional sulfur electrocatalyst with the optimal porous structure for Li–S batteries, pomegranate-like MXene coated TiN microspheres were prepared by the spray-drying method. Specifically, we introduced TiN hollow nanospheres into a three-dimensional layered porous Ti$_3$C$_2$ MXene framework. Compared with the pure three-dimensional MXene microspheres, we proved that TiN hollow nanospheres not only retain the conductivity of MXene skeleton, excellent electron/ion transport properties and adsorption capacity of LiPSs but also have a certain catalytic ability for the conversion of LiPSs to achieve rapid redox reaction. Benefiting from the advantages of the structure and composition, the TiN@MXene cathode displayed large specific capacities and excellent cycling stability with a negligible decay rate of 0.048% per cycle over 1000 cycles at 1C. Even under a high sulfur loading of 5.1 mg cm^{-2}, high capacity retention of 816 mA h g^{-1} was achieved after 200 cycles at 0.2C. This study provides an effective development strategy for the design of multi-functional sulfur electrocatalyst for Li–S batteries, and more importantly, affords sufficient understanding and rational application of the two-dimensional layered materials for related energy storage devices.

Conflicts of interest

There are no conflicts to declare.

Acknowledgements

References

1 J. X. Tu, H. J. Li, T. B. Lan, S. Z. Zeng, J. Z. Zou, Q. Zhang and X. R. Zeng, *J. Alloys Compd.*, 2020, **822**, 153751.

2 D. W. Yang, Z. F. Liang, P. Y. Tang, C. Q. Zhang, M. X. Tang, Q. Z. Li, J. J. Biendicho, J. S. Li, M. Heggen, R. E. Dunin-Borkowski, M. Xu, J. Llorca, J. Arbiol, J. R. Morante, S. L. Chou and A. Cabot, *Adv. Mater.*, 2022, **34**, 2108835.

3 Q. Qi, H. Zhang, P. G. Zhang, Z. H. Bao, W. Zheng, W. B. Tian, W. Zhang, M. Zhou and Z. M. Sun, *2D Materials*, 2020, **7**, 25049.

4 T. L. Huang, Q. Cao, B. Jing, X. Y. Wang, D. Wang and L. B. Liang, *Chem. Eng. J.*, 2022, **430**, 132677.

5 H. Wang, S. A. He, Z. Cui, C. T. Xu, J. Q. Zhu, Q. Liu, G. J. He, W. Luo and R. J. Zou, *Chem. Eng. J.*, 2021, **420**, 129693.

6 R. R. Chu, T. T. Nguyen, Y. Q. Bai, N. H. Kim and J. H. Lee, *Adv. Energy Mater.*, 2022, **12**, 2102805.

7 J. B. Kang, X. H. Tian, C. Z. Yan, L. Y. Wei, L. Gao, J. G. Ju, Y. X. Zhao, N. P. Deng, B. W. Cheng and W. M. Kang, *Small*, 2022, **18**, 2104469.

8 Z. L. Xu, J. K. Kim and K. Kang, *Nano Today*, 2018, **19**, 84–107.

9 L. Huang, S. H. Shen, Y. Zhong, Y. Q. Zhang, L. J. Zhang, X. L. Wang, X. H. Xia, X. L. Tong, J. C. Zhou and J. P. Tu, *Adv. Mater.*, 2022, **34**, 2107415.

10 S. Rehman, T. Y. Tang, Z. S. Ali, X. X. Huang and Y. L. Hou, *Small*, 2017, **13**, 1700087.

11 Z. D. Huang, M. T. Yang, J. Q. Qi, P. Zhang, L. N. Lei, Q. C. Du, L. Bai, H. Fu, X. S. Yang, R. Q. Liu, T. Masese, H. J. Zhang and Y. W. Ma, *Chem. Eng. J.*, 2020, **387**, 124080.

12 W. W. Sun, S. K. Liu, Y. J. Li, D. Q. Wang, Q. P. Guo, X. B. Hong, K. Xie, Z. Y. Ma, C. M. Zheng and S. Z. Xiong, *Adv. Funct. Mater.*, 2022, **32**, 2205471.

13 Y. P. Li, D. Lei, T. Y. Jiang, J. L. Guo, X. Y. Deng, X. Zhang, C. Hao and F. X. Zhang, *Chem. Eng. J.*, 2021, **426**, 131798.

14 W. W. Sun, C. Liu, Y. J. Li, S. Q. Luo, S. K. Liu, X. B. Hong, K. Xie, Y. M. Liu, X. J. Tan and C. M. Zheng, *ACS Nano*, 2019, **13**, 12137–12147.

15 Y. J. Zhang, J. Qu, Q. Y. Ji, T. T. Zhang, W. Chang, S. M. Hao and Z. Z. Yu, *Carbon*, 2019, **155**, 353–360.

16 T. Wang, D. Luo, Y. G. Zhang, Z. Zhang, J. Y. Wang, G. L. Cui, X. Wang, A. P. Yu and Z. W. Chen, *ACS Nano*, 2021, **15**, 19457–19467.

17 H. Tang, W. L. Li, L. M. Pan, C. P. Cullen, Y. Liu, A. Pakdel, D. H. Long, J. Yang, N. McEvoy, G. S. Duesberg, V. Nicolosi and C. F. Zhang, *Adv. Sci.*, 2018, **5**, 1800502.

18 H. Tang, W. Li, L. Pan, K. Tu, F. Du, T. Qiu, J. Yang, C. P. Cullen, N. McEvoy and C. Zhang, *Adv. Funct. Mater.*, 2019, **29**, 1901907.

19 K. R. G. Lim, A. D. Handoko, S. K. Nemani, B. Wyatt, H. Y. Jiang, J. W. Tang, B. Anasori and Z. W. Seh, *ACS Nano*, 2020, **14**, 10834–10864.

20 Y. Z. Wang, T. C. Guo, Z. N. Tian, K. Bibi, Y. Z. Zhang and H. N. Alshareef, *Adv. Mater.*, 2022, **21**, 2108560.

21 M. Q. Zhao, X. Q. Xie, C. E. Ren, T. Makaryan, B. Anasori, G. X. Wang and Y. Gogotsi, *Adv. Mater.*, 2017, **29**, 1702410.

22 D. Z. Wang, Y. Lin, D. W. Hu, P. K. Jiang and X. Y. Huang, *Composites, Part A*, 2020, **130**, 105754.

23 K. Li, M. Y. Liang, H. Wang, X. H. Wang, Y. S. Huang, J. Coelho, S. Pinilla, Y. L. Zhang, F. W. Qi, V. Nicolosi and Y. X. Xu, *Adv. Funct. Mater.*, 2020, **30**, 2070306.

24 L. P. Liao, A. Zhang, K. Zheng, R. Liu, Y. J. Cheng, L. H. Wang, A. H. Li and J. Q. Liu, *ACS Appl. Mater. Interfaces*, 2021, **13**, 28222–28230.

25 L. Y. Xiu, Z. Y. Wang, M. Z. Yu, X. H. Wu and J. S. Qiu, *ACS Nano*, 2018, **12**, 8017–8028.

26 W. G. Lim, C. S. Jo, A. Cho, J. K. Hwang, S. Kim, J. W. Han and J. Lee, *Adv. Mater.*, 2019, **31**, 1806547.

27 X. Huang, J. Y. Tang, T. F. Qiu, R. Knibbe, Y. X. Hu, T. U. Schulli, T. G. Lin, Z. L. Wang, P. Chen, B. Luo and L. Z. Wang, *Small*, 2021, **17**, 2101360.

28 T. Peng, N. Zhang, Y. Yang, M. J. Zhang, R. J. Luo, C. Chen, Y. Lu and Y. S. Luo, *Small*, 2022, **18**, 2202917.

29 Y. Guo, D. Y. Zhang, Y. Yang, Y. B. Wang, Z. X. Bai, P. K. Chu and Y. S. Luo, *Nanoscale*, 2021, **13**, 4624–4633.

30 R. J. Luo, Q. H. Yu, Y. Lu, M. J. Zhang, T. Peng, H. L. Yan, X. M. Liu, J.-K. Kim and Y. S. Luo, *Nanoscale Horiz.*, 2019, **4**, 531–539.

31 H. Y. Wang, L. J. Wang, H. C. Zhang, H. Jiang, C. Z. Li and J. J. Wang, *Chem. Eng. J.*, 2022, **431**, 134179.

32 Y. C. Zhu, K. Rajouâ, S. Le Vot, O. Fontaine, P. Simon and F. Favier, *Nano Energy*, 2020, **73**, 104734.

33 A. S. Levitt, M. Alhabeb, C. B. Hatter, A. Sarycheva, G. Dion and Y. Gogotsi, *J. Mater. Chem. A*, 2019, **7**, 269–277.

34 Z. Y. Xing, G. Li, S. Sy and Z. W. Chen, *Nano Energy*, 2018, **54**, 1–9.

35 L. L. Ma, L. J. Yu, J. C. Liu, Y. Q. Su, S. Li, X. H. Zang, T. Meng, S. H. Zhang, J. J. Song, J. J. Wang, X. X. Zhao, Z. M. Cui, N. Wang and Y. Zhao, *Energy Storage Mater.*, 2022, **44**, 180–189.

36 M. K. Peng, L. Wang, L. B. Li, X. N. Tang, B. Y. Huang, T. Hu, K. Yuan and Y. W. Chen, *Adv. Funct. Mater.*, 2021, **210**, 9524.

37 P. Zhang, R. A. Soomro, Z. R. X. Guan, N. Sun and B. Xu, *Energy Storage Mater.*, 2020, **29**, 163–171.

38 S. L. Zhang, H. J. Ying, R. N. Guo, W. T. Yang and W. Q. Han, *J. Phys. Chem. Lett.*, 2019, **10**, 6446–6454.

39 W. Z. Bao, L. Liu, C. Y. Wang, S. Choi, D. Wang and G. X. Wang, *Adv. Energy Mater.*, 2018, **8**, 1702485.

40 Y. C. Wang, Y. H. Wei, B. Y. Wang, P. Jing, Y. Zhang, Y. Zhang, Q. Wang and H. Wu, *Carbon*, 2021, **177**, 60–70.

41 Z. H. Liu, R. Q. Lian, Z. Wu, Y. J. Li, X. Y. Lai, S. Yang, X. Ma, Y. J. Wei and X. Yan, *Chem. Eng. J.*, 2022, **431**, 134163.

42 J. H. Luo, Y. Wang, Y. J. Mao, Y. Zhang, Y. Su, B. C. Zou, S. X. Chen, Q. Deng, Z. L. Zeng, J. Wang and S. G. Deng, *Chem. Eng. J.*, 2022, **433**, 133549.

43 Y. B. Xiao, S. J. Guo, Y. Ouyang, D. X. Li, X. Li, W. C. He, H. Y. Deng, W. Gong, C. Tan, Q. H. Zeng, Q. Zhang and S. M. Huang, *ACS Nano*, 2021, **15**, 18363–18373.

44 Z. K. Kong, Y. H. Lin, J. W. Hu, Y. L. Wang and L. Zhan, *Chem. Eng. J.*, 2021, 132719.

45 H. Zhang, Q. Qi, P. G. Zhang, W. Zheng, J. Chen, A. G. Zhou, W. B. Tian, W. Zhang and Z. M. Sun, *ACS Appl. Energy Mater.*, 2018, **2**, 705–714.

46 M. L. Zhao, Y. Lu, Y. Yang, M. J. Zhang, Z. J. Yue, N. Zhang, T. Peng, X. M. Liu and Y. S. Luo, *Nanoscale*, 2021, **13**, 13085–13094.

47 C. Q. Zhang, R. F. Du, J. J. Biendicho, M. J. Yi, K. Xiao, D. W. Yang, T. Zhang, X. Wang, J. Arbiol, J. Llorca, Y. T. Zhou, J. R. Morante and A. Cabot, *Adv. Energy Mater.*, 2021, **11**, 2100432.

48 Y. Lu, M. L. Zhao, Y. Yang, M. J. Zhang, N. Zhang, H. L. Yan, T. Peng, X. M. Liu and Y. S. Luo, *Nanoscale Horiz.*, 2022, **7**, 543–553.

49 S. Y. Zhao, H. Y. Pei, Q. Yang, K. L. Liu, Y. Y. Huang, Z. Wang, G. S. Shao, J. P. Liu and J. L. Guo, *Nano Res.*, 2022, **11**, 5974.

50 K. Z. Li, J. Luo, L. H. Dong, G. Q. Yuan, W. Lei, Q. L. Jia, H. J. Zhang and S. W. Zhang, *Ceram. Int.*, 2022, **48**, 19017–19025.

51 K. K. Gao, R. Xu, Y. X. Chen, Z. T. Zhang, J. S. Shao, H. P. Ji, L. Y. Zhang, S. S. Yi, D. L. Chen, J. H. Hu and Y. F. Gao, *Chin. Chem. Lett.*, 2023, **34**, 107229.

52 W. Y. Lieu, D. L. Fang, Y. J. Li, X. L. L. Li, C. J. Lin, A. Thakur, B. C. Wyatt, S. N. Sun, T. Ghosh, B. Anasori, M. F. Ng, H. Y. Yang and Z. W. Seh, *Nano Lett.*, 2022, **22**, 8679–8687.

53 R. H. Hou, S. J. Zhang, P. Zhang, Y. S. Zhang, X. L. Zhang, N. Li, Z. H. Shi and G. S. Shao, *J. Mater. Chem. A*, 2020, **8**, 25255–25267.